

Quantized Ballistic Transport of Electrons and Electron Pairs in $\text{LaAlO}_3/\text{SrTiO}_3$ Nanowires

Anil Annadi^{1,2}, Guanglei Cheng^{1,2,4}, Hyungwoo Lee³, Jung-Woo Lee³, Shicheng Lu^{1,2},
Anthony Tylan-Tyler^{1,2}, Megan Briggeman^{1,2}, Michelle Tomczyk^{1,2}, Mengchen Huang^{1,2},
David Pekker^{1,2}, Chang-Beom Eom³, Patrick Irvin^{1,2}, Jeremy Levy^{1,2*}

¹Department of Physics and Astronomy, University of Pittsburgh, Pittsburgh, PA 15260, USA.

²Pittsburgh Quantum Institute, Pittsburgh, PA, 15260 USA.

³Department of Materials Science and Engineering, University of Wisconsin-Madison, Madison, WI 53706, USA.

⁴CAS Key Laboratory of Microscale Magnetic Resonance and Department of Modern Physics, University of Science and Technology of China, Hefei 230026, China

* jlevy@pitt.edu

Abstract

SrTiO₃-based heterointerfaces support quasi-two-dimensional (2D) electron systems that are analogous to III-V semiconductor heterostructures, but also possess superconducting, magnetic, spintronic, ferroelectric and ferroelastic degrees of freedom. Despite these rich properties, the relatively low mobilities of 2D complex-oxide interfaces appear to preclude ballistic transport in 1D. Here we show that nearly ideal 1D electron waveguides exhibiting quantized ballistic transport of electrons and (non-superconducting) electron pairs can be formed at the interface between the two band insulators LaAlO₃ and SrTiO₃. These electron waveguides are created using a well-established conductive atomic-force microscope (c-AFM) lithography technique that enables nanoscale control of the metal-insulator transition at the LaAlO₃/SrTiO₃ interface. Quantized ballistic transport within conducting nanowires at low temperature ranges from truly single-mode (1D) to three-dimensional (3D), depending on the applied magnetic field and gate voltage. Quantization of the lowest e^2/h plateau indicate a ballistic mean-free path $l_{MF} \sim 20 \mu\text{m}$, roughly an order of magnitude larger than in III-V nanowires. Non-superconducting electron pairs are found to be stable in magnetic fields as high as $B = 11 \text{ T}$, and propagate ballistically with quantized conduction $2e^2/h$. Theories of one-dimensional (1D) transport of interacting electron systems depend crucially on the sign of the electron-electron interaction, which may help explain the highly ballistic transport behavior. The 1D geometry yields new insights into the electronic structure of the LaAlO₃/SrTiO₃ system and offers a new platform for the study of strongly interacting 1D electronic systems.

INTRODUCTION

Dimensionality has a profound effect on electron transport. When electrons are confined in two dimensions (2D), new phases such as the integer (1) and fractional (2) quantum Hall effect emerge. Electrons confined in one dimension (1D) lose nearly all of their recognizable features (3, 4). For example, the electron spin and charge can separate and move independently of one another (5), and the charge itself can fractionalize (6). However, in 1D, the conductance remains quantized in units of e^2/h (7). The edges of 2D quantum Hall systems form nearly-ideal 1D channels, where magnetic confinement gaps out the 2D bulk and protects electrons from back-scattering. The chiral edge transport of the quantum Hall phase is fundamentally different from transport in 1D nanostructures where electrons are electrostatically confined to a narrow channel. Quasi-1D transport was first reported in narrow constrictions, also known as “quantum point contacts” (8, 9). The conductance through these narrow channels is given by the number of allowed transverse modes, which is tunable by an external gate. The confined regions are generally short, of the order 100-200 nm, with a channel length set by the distance between the top gate electrodes and the high-mobility buried layer. There have been many attempts to engineer more extended 1D quantum wires using other growth techniques and different materials. For example, cleaved-edge overgrown III-V quantum wires exhibit quantized transport in devices as long as 2 μm (10). Other one-dimensional systems include carbon nanotubes (11), graphene nanoribbons (12), and compound semiconductor nanowires (10, 13). In all of these systems, electron transport is sensitive to minute amounts of disorder. For example, when 2D semiconductor heterostructures are patterned into 1D channels, the mobility drops tremendously (14). Theoretically, this sensitivity to disorder can be understood within the framework of Tomonaga-Luttinger liquid theory, which predicts that repulsive interactions

promote full backscattering from even a single weak impurity (15, 16). Conversely, attractive interactions are predicted to strongly suppress impurity scattering (16, 17).

Oxide heterostructures have added new richness to the field of quantum transport in the last decade. For example, ZnO/(Mn,Zn)O heterostructures have achieved sufficiently high mobility to reveal fractional quantum Hall states (18), which has revealed new even-denominator states not visible in III-V hosts (19). LaAlO₃/SrTiO₃ heterostructures (20) exhibit a wide range of behavior including gate-tunable conducting (21), superconducting (22), ferromagnetic (23), and spin-orbit coupled (24-27) phases. As interesting and rich as its palette of phases may be, the 2D electron mobility is still low ($\mu \sim 10^3$ cm²/Vs) compared with high-mobility GaAs/AlGaAs heterointerfaces ($\mu \sim 10^7$ cm²/Vs). However, despite the modest mobility of the LaAlO₃/SrTiO₃ 2D interface, there is an increasing body of evidence suggesting that 1D geometries are able to support ballistic transport (24-27).

Landauer's Formula

Transport through a coherent quantum conductor can be described by Landauer's formula, $G = (e^2/h) \sum_i T_i(\mu)$, where each energy subband available at chemical potential μ contributes one quantum of conductance e^2/h with transmission probability $T_i(\mu)$. The transmission probability is given by $T_i(\mu) = \bar{T} F_T(\mu - E_i)$ where \bar{T} encompasses any tunneling resonances, cavity interference effects, or backscattering processes, $F_T(E)$ is a thermal broadening from the Fermi distribution function of the leads at a finite temperature, and E_i represents the energy minimum of the i^{th} electron subband (28). Within this framework, the conductance increases in steps of e^2/h every time the chemical potential crosses a subband energy minimum. Transport through the channel is ballistic and dissipationless; however, the measured resistance is given by $R = h/(Ne^2)$, where N is the

number of occupied subbands. The apparent contradiction between dissipationless transport within the waveguide and finite resistance was understood by Landauer, and put on a rigorous footing by Maslov and Stone, who developed a Luttinger liquid model of energy dissipation within the leads (29). However, in experiments, even the cleanest systems do not have infinite scattering lengths; each subband can backscatter electrons, leading to a suppression which can be modeled as $\bar{T} = \exp\left(-\frac{L}{L_i}\right)$ (30), where L is the channel length and L_i is the mode-dependent scattering length. When $L_i \sim L$, the system is in the ballistic or quasi-ballistic regime, and when $L_i \gg L$, the system enters a quantized ballistic regime.

Electron Waveguide

The expected properties of an ideal few-mode (i.e., few-subband) electron waveguide are illustrated in Figure 1. The conductance of the waveguide depends on the number of accessible quantum channels (shown in Figure 1D-E as energy-shifted parabolic bands). Figure 1B, D depicts a state in which a single spin-resolved subband is occupied. As the chemical potential μ is increased, more subbands in the waveguide become occupied. Figure 1C and Figure 1E depict a state in which $N = 3$ subbands contribute to transport. Each spin-resolved subband contributes e^2/h to the total conductance (Figure 1F). The energy at which μ crosses a new subband (at $k_x = 0$) can generally shift in an applied magnetic field due to Zeeman and orbital effects. When lateral and vertical confinement energies are comparable, a more complex subband structure can emerge, as illustrated in Figure 1G.

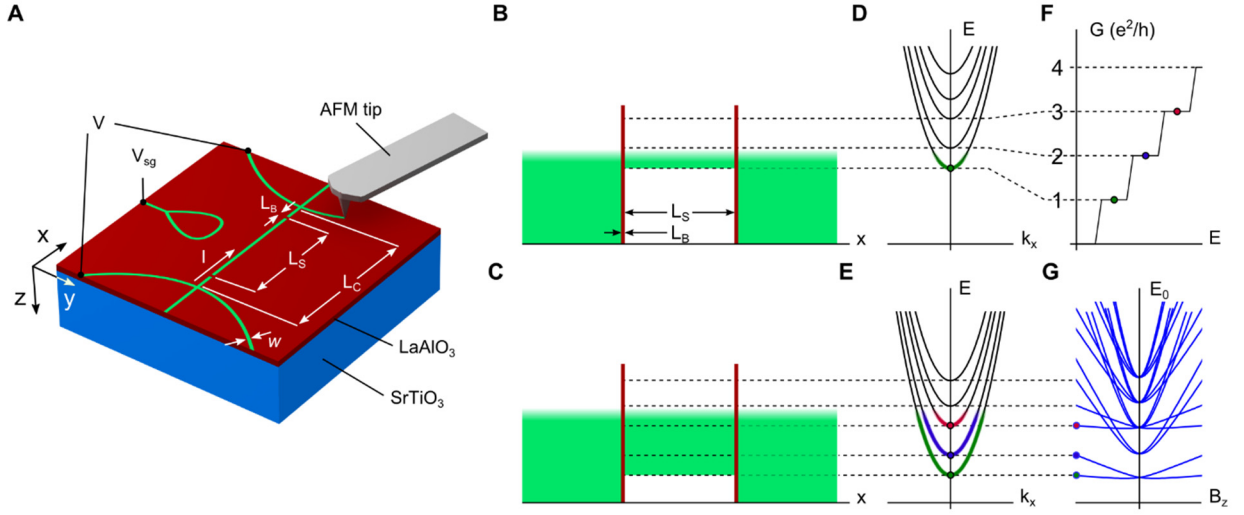


Figure 1. Expected transport characteristics of electron waveguides. (A) Schematic of LaAlO₃/SrTiO₃ electron waveguides fabricated by c-AFM lithography. Two barriers, with width $L_B \sim 5 - 10$ nm and spacing $L_S \sim 10 - 1000$ nm, formed by negative AFM tip pulses, surround the main channel of length $L_C \sim 500 - 1800$ nm, enabling the subbands in the waveguide to be tuned by V_{sg} . (B and C) Energy diagrams of the waveguide for two different values of chemical potential μ , which is controlled by V_{sg} . For (B), a single subband is occupied, while for (C) three subbands are occupied. (D and E) depict the corresponding energy subbands corresponding to (B) and (C). Thick colored bands indicate occupied states. (F) Zero-bias conductance quantization as a function of chemical potential. (G) Waveguide subband structure (with both lateral and vertical confinement) as a function of magnetic field (which couples to the electrons via both Zeeman and orbital effect) and chemical potential.

RESULTS

Quantized ballistic transport of electrons in LaAlO₃/SrTiO₃ waveguides

Here we fabricate LaAlO₃/SrTiO₃ electron waveguides using a well-established conductive atomic-force microscopy (c-AFM) lithography technique (31, 32), as shown in Figure 1A (also see Materials and Methods). The experimentally measured conductance of LaAlO₃/SrTiO₃ waveguides is shown in Figure 2A-D. We focus on two distinct devices: device A ($L_C = 500$ nm, $L_S = 50$ nm, $L_B = 20$ nm) and device B ($L_C = 1.8$ μ m, $L_S = 1$ μ m, $L_B = 20$ nm). Figure 2A, C shows the zero-bias conductance $G = dI/dV$ as a function of side-gate voltage V_{sg} (or chemical potential μ for a sequence of magnetic fields between $B = 0$ T and 9 T. (Analysis of the non-equilibrium conductance, described in 0,

enables the lever-arm ratio $\alpha \equiv d\mu/dV_{sg}$ and g-factor $g \equiv \mu_B^{-1} d\mu/dB$, where μ_B is the Bohr magneton for the two devices A (B), to be extracted: $\alpha_{A(B)} = 4.5$ (9.9) $\mu\text{eV/mV}$ and $g_{A(B)} = 0.6$ (0.6). For Device A (Figure 2A), clear conductance steps of $G = 2e^2/h$ are visible for magnetic fields above ~ 1 T. These steps split into e^2/h steps, up to $N = 6$, at fields above ~ 3 T. These electron waveguides exhibit no valley degeneracies and can be tuned to the lowest spin-polarized conduction plateau ($G = e^2/h$), with no signatures of sub-structure or “0.7 anomalies” (33). When only a single barrier is present, no conduction quantization is observed (see discussion in Supporting Information and Figure S5) because the tunneling barriers are extremely narrow, in contrast to traditional semiconductor heterostructures.

We attribute the observed conduction plateaus to Landauer quantization (7), for which the total conductance depends on the number of available quantum channels (subbands). The subband structure of these $\text{LaAlO}_3/\text{SrTiO}_3$ electron waveguides is clearly revealed by examining the transconductance $dG/d\mu$ as a function of μ and external magnetic field B (Figure 2B, D). The transconductance shows an intricate set of bands (bright areas) which mark the boundaries where new subbands become available (as illustrated in Figure 1G). These bands are separated by dark areas ($dG/d\mu \rightarrow 0$) where the conductance is highly quantized. At low magnetic fields (and low μ), the subbands scale roughly as B^2 and become more linear at larger magnetic fields. A pattern of subbands repeats at least twice, spaced by approximately $500 \mu\text{eV}$. The transconductance of the two devices A ($L_S = 50 \text{ nm}$) and B ($L_S = 1 \mu\text{m}$) are remarkably similar, despite the large difference in channel length and the fact that the coupling constant for the two devices differs by a factor of two.

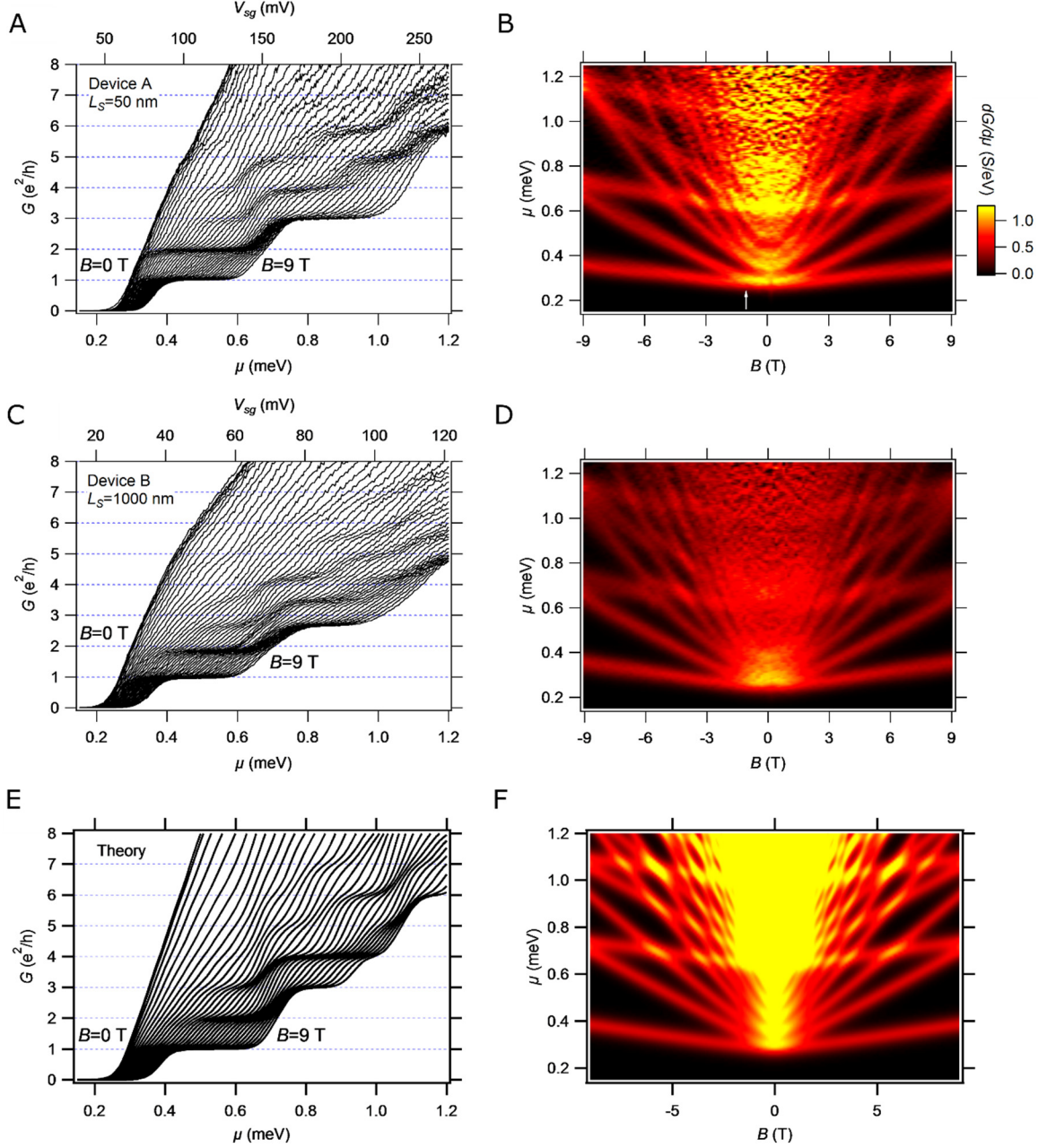


Figure 2. Conductance and transconductance of devices A and B, and comparison with theory. (A and C) Zero-bias conductance of device A ($L_B = 20$ nm, $L_C = 500$ nm, $L_S = 50$ nm) and device B ($L_B = 20$ nm, $L_C = 1,800$ nm, $L_S = 1,000$ nm) as a function of chemical potential μ and magnetic fields B in the range 0-9 T. (B and D) Transconductance $dG/d\mu$ shown as a function of μ and B for device A (B) and device B (D). Each bright band marks the crossing of a subband, and the white arrow in (B) indicates the pairing field $B_P \approx 1$ T. The revealed subband structures show remarkable similarity between these two devices. (E) Theoretical zero-bias conductance curves, modeling device A, for a non-interacting channel as a function of the chemical potential and magnetic field. (F) Corresponding transconductance $dG/d\mu$ as a function of μ and B . Transitions have been broadened by a 65 μ eV-wide Lorentzian.

While the lowest $N = 1$ state remains highly quantized for both devices (see Figure 2), the plateaus do not fully reach the integer values for higher N for device B. The relationship between two length scales—the length scale of the device and the elastic scattering length (which is typically much shorter than the inelastic scattering length in quantum devices) — determines whether transport is ballistic. The conductance of these modes are not exactly e^2/h , however, in part because they are not topologically-protected edge modes, nor are they quantum Hall edge states. In electron waveguides at the $\text{LaAlO}_3/\text{SrTiO}_3$ interface, the elastic scattering length can be estimated assuming an exponential decay of the conductance $G = G_0 \exp(-L/L_0)$, where L_0 is the scattering length and L is the length of the device. The location of the minimum in the transconductance is used to find the value of the plateaus, as seen in Figure S2. The scattering lengths greatly exceed the length of the devices (**Table S**), implying that the transport is fully ballistic. The error estimate for Device A is limited by the short length of the channel. For Device B, the channel length is long enough to yield (with 10% accuracy) a measure of the scattering length which more than an order magnitude larger than for any nanowire created from a III-V semiconductor. We also note that systematic errors (e.g., reflections of incident electrons at one or both of the barriers) are only expected to increase these estimates.

Non-interacting waveguide model

Many of the features in the transconductance spectra shown in Figure 2A-D are captured by a waveguide model of non-interacting electrons in a 3D waveguide. The waveguide's confining potential can be regarded as translationally invariant along the propagation direction (x) and convex along the two transverse directions (lateral y and vertical z). Since the measured carrier density in conductive nanostructures created by c-

AFM lithography is typically in the range of $0.5 - 1.0 \times 10^{13} \text{ cm}^{-2}$ (34), only the Ti d_{xy} band, being lower in energy than the d_{xz} and d_{yz} bands at the $\text{LaAlO}_3/\text{SrTiO}_3$ interface (35), is expected to be occupied at these carrier densities. Thus we assume that all of the conducting channels are derived from the lower d_{xy} band.

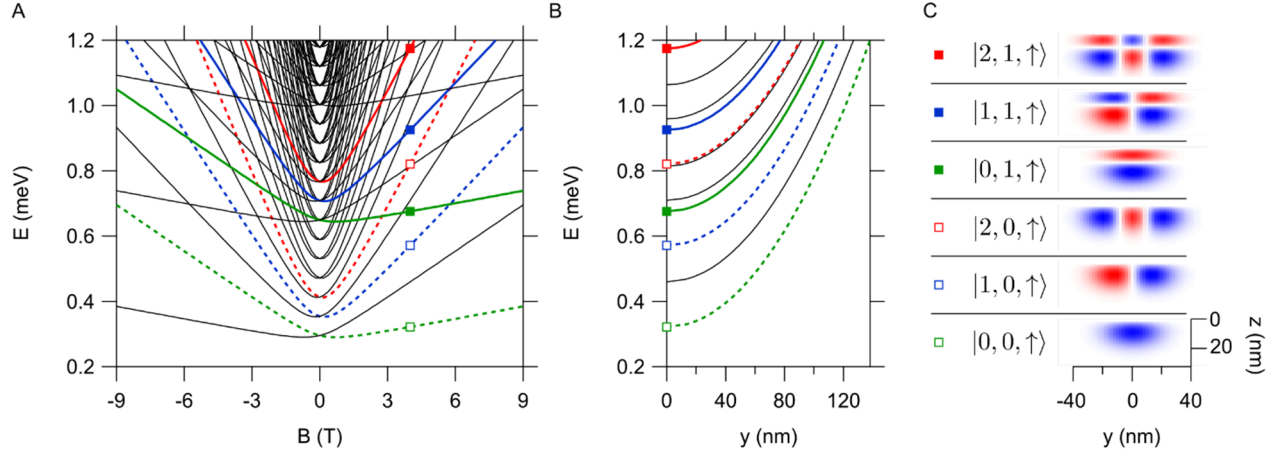


Figure 3. Non-interacting waveguide model. (A) Eigenenergies for a quantum wire for the Hamiltonian described in Eq. (1) are plotted as a function of magnetic field B . Selected spin-up states are highlighted in color. (B) Magnetically induced displacement of these states along the y direction as a function of eigenstate energy for $B = 4$ T. (C) Six corresponding wavefunctions, labeled by $|n, m, s\rangle$, at $k_x = 0$ and $B = 4$ T. Red and blue colors indicate opposite sign of the wavefunction.

We use a potential $U_y = \frac{1}{2}m_y^*\omega_y^2y^2$ to describe the lateral confinement, where $m_x^* = m_y^*$ is the effective mass in the x - y plane and $\omega_y = \frac{\hbar}{m_y^*\ell_y^2}$ is the confinement frequency with ℓ_y being the characteristic width of the waveguide. In the vertical direction, the confinement at the interface is modeled by a half-parabolic potential, namely, $U_z = \frac{1}{2}m_z^*\omega_z^2z^2$ for $z > 0$ and $U_z = +\infty$ for $z \leq 0$, where $\omega_z = \frac{\hbar}{m_z^*\ell_z^2}$ is the confinement frequency, m_z^* is the effective mass of the d_{xy} band in the z direction, and ℓ_z is the

penetration depth into the SrTiO₃. Within this single-particle picture, the full Hamiltonian can be written in the Landau gauge as

$$H = \frac{(p_x - eBy)^2}{2m_x^*} + \frac{p_y^2}{2m_y^*} + \frac{p_z^2}{2m_z^*} + \frac{m_y^* \omega_y^2}{2} y^2 + \frac{m_z^* \omega_z^2}{2} z^2 - g \frac{\mu_B}{2} B \sigma_z, \quad (1)$$

where σ_z is the Pauli matrix. This Hamiltonian is readily solved to yield energy eigenstates $|n, m, s\rangle \otimes |k_x\rangle$ with corresponding energy

$$E_{m,n,s,k_x} = \hbar \Omega \left(n + \frac{1}{2} \right) + \hbar \omega_z \left((2m + 1) + \frac{1}{2} \right) - g \mu_B B s + \frac{\hbar^2 k_x^2}{2m_x^*} \left(1 - \frac{\omega_c^2}{\Omega^2} \right), \quad (2)$$

where $\omega_c = \frac{eB}{m_y^*}$ is the cyclotron frequency, $\Omega = \sqrt{\omega_y^2 + \omega_c^2}$ is the effective frequency of the waveguide and magnetic field, n (m) enumerates the lateral (vertical) states, and $s = \pm 1/2$ is the spin quantum number. Distinct spin-resolved subbands (36) are associated with the discrete quantum numbers $|n, m, s\rangle$. Figure 3A plots the eigenenergies for parameters that have been adjusted to resemble the experimentally measured transconductance (Figure 2D). These values are also used to compute the expected conductance and transconductance versus chemical potential (Figure 2E, F). The corresponding wavefunctions $\phi_{n,m,k_x,s}(y, z)$ (defined in Eq. (3) for selected states are illustrated in Figure 3C:

$$\begin{aligned}
\phi_{n,m,k,s}(y,z) &\equiv \langle y,z,s;k|n,m,s\rangle \otimes |k_x\rangle \\
&= N_{n,m,k} e^{-\frac{m_y^* \Omega}{2\hbar} \left(y - \frac{\hbar \omega_c^2}{m_y^* \Omega} k\right)^2} H_n \left(\sqrt{\frac{m_y^* \Omega}{\hbar}} \left(y - \frac{\hbar \omega_c^2}{m_y^* \Omega} k\right) \right) \\
&\quad e^{-\frac{m_z^* \omega_z}{2\hbar} z^2} H_{2m+1} \left(\sqrt{\frac{m_z^* \omega_z}{\hbar}} z \right).
\end{aligned} \tag{3}$$

Here, $H_n(x)$ are the Hermite polynomials. The wavefunctions are displaced laterally by the magnetic field by an amount that depends quadratically on the kinetic energy (Figure 3B). The set of parameters for device A (B), $\ell_y = 26$ (27) nm, $\ell_z = 8.1$ (7.9) nm, $m_x^* = m_y^* = 1.9$ (1.8) m_e , and $m_z^* = 6.5$ (6.4) m_e is obtained by maximizing agreement with a tight-binding model that includes spin-orbit interactions (see Supporting Information). At low magnetic fields, the energy scales quadratically with magnetic field, as it is dominated by the geometrical confinement contribution; at higher magnetic fields, the confinement from the cyclotron orbits dominates, producing a linear scaling. The crossover occurs near $\omega_B = \frac{eB}{m_y^*} \sim \omega_y$.

Electron pairs at low magnetic fields

While the single-particle model captures the overall subband structure, clear deviations in the experimental results are apparent. These electron waveguides exhibit electron pairing without superconductivity below a critical magnetic field B_p , similar in nature to reports for strongly confined quantum dot structures (37). The extracted pairing field for the $|0,0,s\rangle$ states is $B_p \approx 1$ T for device A and B (see Figure 2). In other devices, electron pairing is much stronger. Device C, written on a different sample, exhibits highly quantized conduction but with a subband structure that differs qualitatively from devices A

and B. There are three pairs of subbands that generate $2e^2/h$ steps (Figure 4A). These pairs unbind at a critical field $B_p \approx 11$ T (Figure 4C, dashed lines). Superimposed over these pairs is a separate subband (with higher curvature) that contributes e^2/h to the conductance (Figure 4B). At $B \approx 3$ T two paired subbands are superimposed with the unpaired subband, leading to a plateau near $5e^2/h$ (highlighted in green). Finally, re-entrant electron pairing is observed when electron subbands become degenerate.

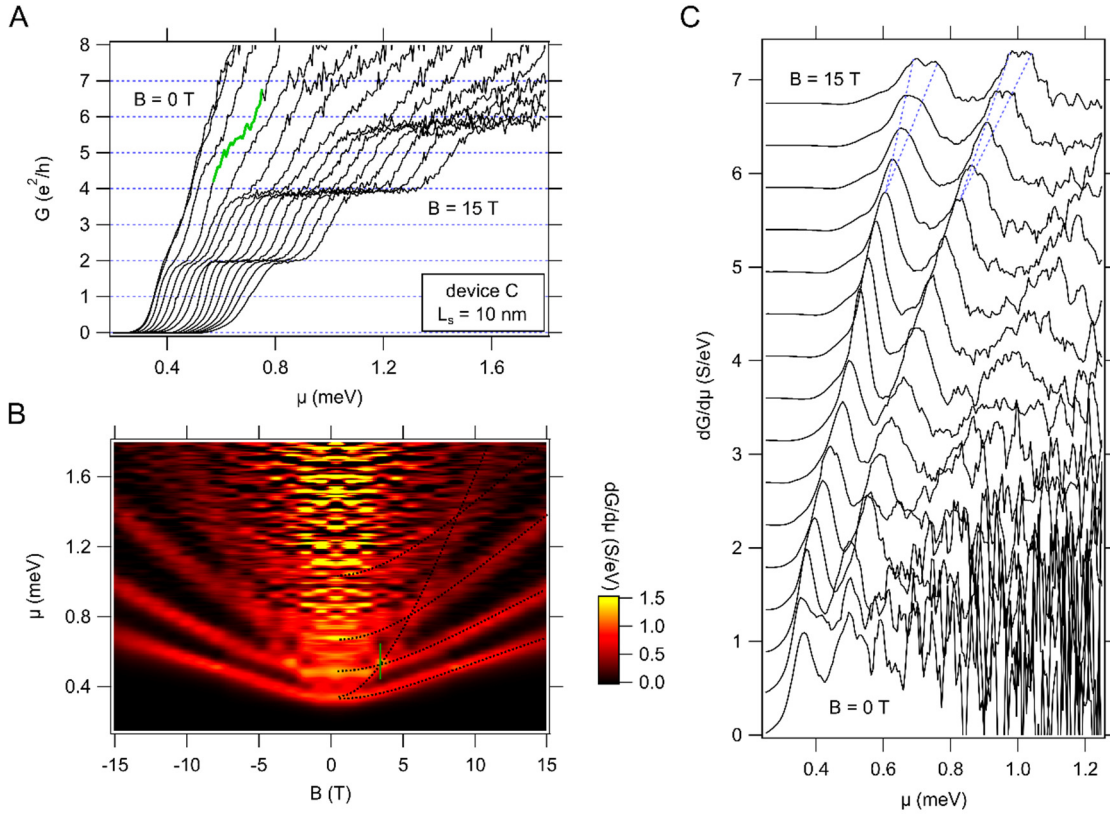


Figure 4. Strongly paired electron waveguides. (A) Conductance of device C ($L_B = 5$ nm, $L_C = 350$ nm, $L_S = 10$ nm) versus chemical potential for magnetic fields ranging from 0 T to 15 T. This device shows strong electron pairing and associated $2e^2/h$ conductance steps. (B) Transconductance plot shows three strongly paired states and a superimposed state with higher curvature associated with a conductance of e^2/h . The value of the later state can be seen at $B = 3$ T in the conductance curve in panel a (highlighted in green) where it combines with the second strongly paired subband into a plateau near $5e^2/h$. (C) Linecuts of transconductance plotted at magnetic fields from 0 T to 15 T in 1 T steps. The $2e^2/h$ peaks split above a pairing field $B_p \approx 11$ T, as indicated by the dashed lines.

Re-entrant pairing

Deviations from the single particle model arise from electron-electron interactions within the waveguide. The effects of these interactions become apparent in the transconductance data in the vicinity of subband crossing points (both at zero magnetic field and at finite field). Specifically, we observe extended regions of $2e^2/h$ conductance steps which we associate with a transition from a vacuum phase directly into a paired phase. That is, when a pair of subbands with opposite spin (e.g. $|1,0,\uparrow\rangle$ and $|0,1,\downarrow\rangle$) intersect at a finite magnetic field they are found to pair re-entrantly before separating again (Figure 5). This observation is consistent with previously studies of one dimensional fermions with attractive interactions using both the Bethe Ansatz approach (38) (for the case of equal masses) and numerical approaches (39, 40) (for the case of unequal masses).

Self-consistent Hartree-Bogoliubov model

Here, we present a simple self-consistent Hartree-Bogoliubov model of crossing subbands that is both consistent with the more refined approaches and highlights the relevant physics without added complication. We start with the two-band, one-dimensional Hubbard model:

$$H = - \sum_{i,\alpha} t_{\alpha} (c_{\alpha,i}^{\dagger} c_{\alpha,i+1} + h.c.) + \sum_{i,\alpha} V_{\alpha}(V_{sg}, B) n_{\alpha,i} + U \sum_i n_{1,i} n_{2,i}, \quad (4)$$

where i is the site index, α is the subband index, $V_{\alpha}(V_{sg}, B)$ describes the electrochemical potential as a function of the side gate voltage and magnetic field, and $U < 0$ models the

electron-electron attraction. At the mean field level, this model is described by the single-particle Hamiltonian

$$\begin{pmatrix} \xi_{1,k} + \Sigma_1 & 0 & 0 & \Delta_{rp} \\ 0 & -(\xi_{1,k} + \Sigma_1) & \Delta_{rp} & 0 \\ 0 & \Delta_{rp} & \xi_{2,k} + \Sigma_2 & 0 \\ \Delta_{rp} & 0 & 0 & -(\xi_{2,k} + \Sigma_2) \end{pmatrix} \psi_{\beta,k} \quad (5)$$

$$= E_{\beta,k} \psi_{\beta,k},$$

where we use the $\{c_{1,k}, c_{1,k}^\dagger, c_{2,-k}, c_{2,-k}^\dagger\}$ basis, $\{1,2\}$ are the subband labels, $\psi_{\beta,k}$ and $E_{\beta,k}$ are the quasi-particle wave functions and eigenenergies, $\xi_{\alpha,k}(\mu, B)$ corresponds to the non-interacting energy of an electron in the transverse subband α with momentum k along the wire, in magnetic field B , and chemical potential μ (that is tuned by V_{sg}). $\Sigma_1, \Sigma_2, \Delta_{rp}$ are the mean fields that must be found self-consistently. Σ_α represents the Hartree shifts due to the electrons in the opposite subband $\bar{\alpha}$:

$$\Sigma_\alpha = U_H \int \frac{dk}{2\pi} \langle c_{\bar{\alpha},k}^\dagger c_{\bar{\alpha},k} \rangle \quad (6)$$

and Δ_{rp} represents the re-entrant pairing field

$$\Delta_{rp} = U_B \int \frac{dk}{2\pi} \langle c_{2,-k} c_{1,k} \rangle. \quad (7)$$

For concreteness, we have made the minimal assumption that the interactions are momentum-independent (i.e. local in real space) when writing the mean fields. We caution that a nonzero value of Δ should not be interpreted as a signature of superconductivity but only as a signature of pair formation as we are working in one dimension. Finally, when computing the matrix elements, we must keep in mind that the basis we are using is twice

as big as the physical basis and consequently, quasi-particle wave functions come in conjugate pairs. Only one member of the pair should be used (e.g. the one that has the positive eigenvalue and thus corresponds to the quasi-particle creation operator).

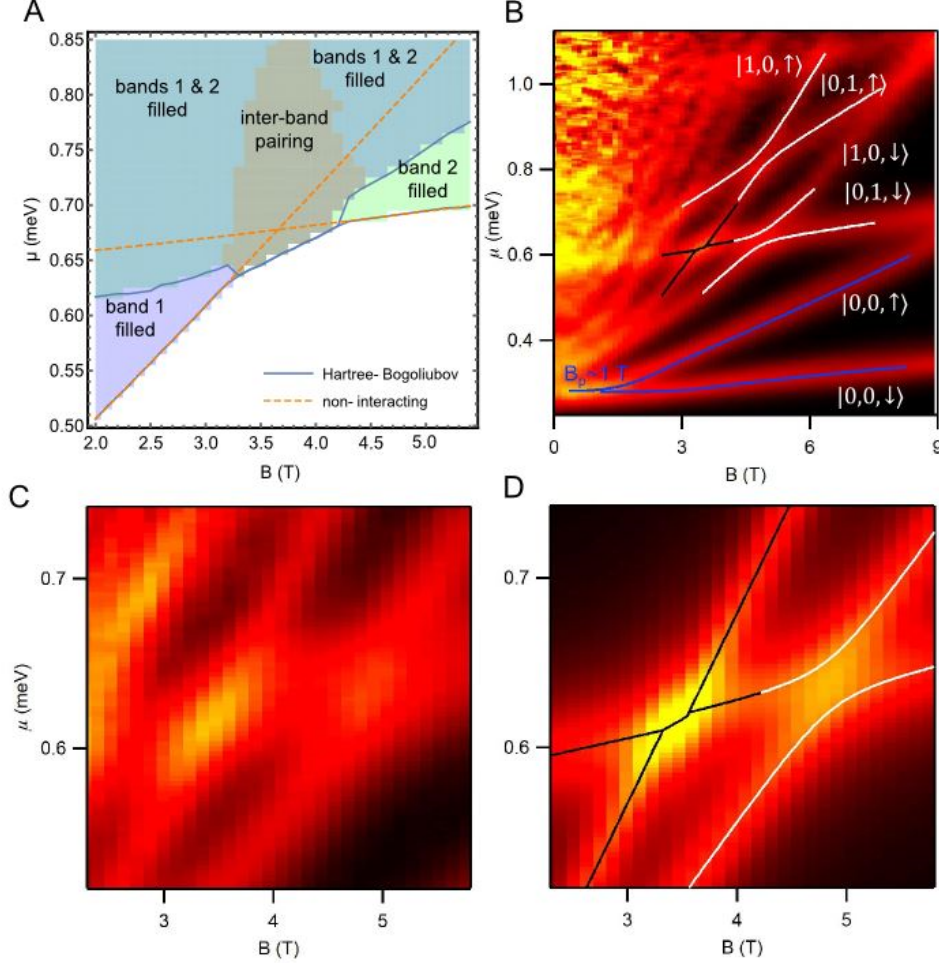


Figure 5. Electron-electron interactions in electron waveguides. (A) Phase diagram of the Hartree-Bogoliubov model in the $\mu - B$ plane and near the crossing point of $|0,1,\downarrow\rangle$ and $|1,0,\uparrow\rangle$. In producing this diagram, we used the band parameters for device A and set the attractive interaction constants to be $U_H = U_B = 100 \mu\text{eV}$. (B) Electron pairing (blue lines), avoided crossing (white lines), and re-entrant pairing (black lines) fittings of device A. (C) Detailed view of re-entrant pairing and avoided crossing data in (B). (D) Combined model fitting of data shown in (C). Here the black lines show the fitting of re-entrant pairing between subband $|0,1,\downarrow\rangle$ and $|1,0,\uparrow\rangle$, with $\Delta_{rp} = 13 \mu\text{eV}$. The white lines are the fitting to the avoided crossing between subband $|0,1,\downarrow\rangle$ and $|1,0,\downarrow\rangle$, with $\Delta_{1,2} = 16 \mu\text{eV}$. (Full set of fitting parameters are listed in Table 1 and Table S2).

We solve the Hartree-Bogoliubov model self-consistently to obtain a phase diagram near the crossing point of the $|0,1,\downarrow\rangle$ and $|1,0,\uparrow\rangle$ subbands (Figure 5A). The locations of

the non-interacting subbands are plotted with dashed lines. By turning on the attractive inter-subband interaction, the Hartree shift tends to pull down the upper subband away from the crossing point; and pairing prevails closer to the crossing point which results in the merger of the two subbands into a single paired subband. Following the Maslov and Stone theorem, the conductance in the paired (spin-gapped) phase must be $2e^2/h$ (41). We expect that these qualitative predictions are generic for systems with attractive inter-band interactions and not particularly sensitive to the assumptions that we have made: i.e. using the Hartree-Bogoliubov model with local interactions.

Table 1. Re-entrant pairing fitting parameters for device A and B.

Device	Subbands	k ($\mu\text{eV/T}$)	b (μeV)	Δ_{rp} (μeV)
Device A	$ 1,0,\uparrow\rangle$	133	168	13
	$ 0,1,\downarrow\rangle$	15	566	
Device B	$ 1,0,\uparrow\rangle$	130	120	10
	$ 0,1,\downarrow\rangle$	14	585	

Provided the phase diagram in Figure 5A, we use a phenomenological model containing the phase boundaries to describe inter-band re-entrant pairing. The basic scenario is when two subbands $E_1(=k_1B+b_1)$ and $E_2(=k_2B+b_2)$ with opposite spins are tuned closely in energy, they combine as an electron pair, which breaks when the energies are tuned further away. These two subbands would simply cross (orange dashed lines) if there were no electron-electron interaction. In the presence of the attractive pairing interaction, the higher energy subband undergoes an energy shift of $-2\delta_{1(2)}$ so that it can be written as $E'_{1(2)} = k_{1(2)}B + b_{1(2)} - 2\delta_{1(2)}$. And a middle section representing the paired phase emerges. The re-entrant pairing energy Δ_{rp} can then be extracted: $\Delta_{rp} = \delta_1 + \delta_2$. We are

now able to use this model to extract these parameters from the experimental data using the fittings shown in Figure 5D. This process then gives a pairing field range $3.3 \text{ T} < B < 3.5 \text{ T}$ and a pairing energy $\Delta_{\text{rp}} = 13 \text{ } \mu\text{eV}$ for subbands $|1,0,\uparrow\rangle$ and $|0,1,\downarrow\rangle$ in device A (see Table 1 for the full fitting parameters).

DISCUSSION

Comparison of observed conductance steps with quantum Hall effect

The observed conductance plateaus are not consistent with a quantum Hall state. The integer quantum Hall effect is defined by an insulating 2D bulk with chiral edge states that are responsible for the quantized conductance. By contrast, $\text{LaAlO}_3/\text{SrTiO}_3$ -based electron waveguides lack the insulating bulk region that prevents backscattering. That is to say, the magnetic length ($\ell_B \sim 15 \text{ nm}$ for $B = 3 \text{ T}$) and the confinement length ($\ell_y = 26 \text{ (27) nm}$ for device A (B)) are comparable and no well-defined bulk region is present.

The 3D structure of the electron waveguides is also inconsistent with quantum Hall physics. The cross-section of our waveguides is ellipsoidal with an aspect ratio of 0.5 (vertical/lateral, see Figure 3C, which is well within the 3D regime. This regime is not expected to support stable quantum Hall bilayer states as multiple vertical subbands are occupied. For example, in Figure 5B, the $|0,0,\uparrow\rangle$ and $|0,1,\downarrow\rangle$ subbands would be unstable and therefore not quantized in a quantum Hall regime, according to Ref. (42). The fact that quantized transport is observed provides further proof that this form of transport is not described by quantum Hall effects.

Finally, the lack of observable quantization at low fields is a consequence of the close spacing of lateral subband modes. The single-particle theory, illustrated in Figure 2E, F, shows that broadening of the subband transitions prevents the individual subbands from

becoming resolvable at low magnetic fields; however, they become visible as soon as the magnetic dispersion can clearly separate them in energy. In other waveguides with larger subband spacing, conductance quantization is observable at small magnetic fields (Figure S4).

Quantized conductance of electron pairs

The observation of quantized conduction in the paired regime ($G = 2e^2/h$ and $|B| < B_p$) signifies that these (non-single-particle) states propagate ballistically, forming an extended state in which electron pairs are bound together while the center-of-mass coordinate remains delocalized. Conduction quantization with steps of $2e^2/h$, rather than $(2e)^2/h$, is consistent with the notion that dissipation takes place not within the channel itself but in the leads, and that electron pairs unbind before they dissipate energy (43, 44). This interpretation is also consistent with the theorem of Maslov and Stone, who argued that the conductance of a Luttinger liquid is determined by the properties of the leads (41). Specifically, the charge conductance of the channel remains $2e^2/h$ when a spin (i.e. pairing) gap is opened in the channel.

Previous reports of electron pairing in confined 1D structures (37) revealed a range of pairing fields that is consistent with the variation observed in these electron waveguides. For device A and B, $B_p \approx 1$ T is relatively low compared to $B_p \approx 11$ T in device C. Figure S4 shows additional variation of B_p in two other devices. No specific dependence of B_p on device length can be inferred. Clearly, there are hidden variables that regulate the strength of electron pairing that have yet to be revealed experimentally.

CONCLUSION

The experiments described here show that electron waveguides provide remarkably detailed insight into the local electronic structure of these oxide interfaces. The level of reproducibility and reconfigurability illustrated by these experiments represents a significant advance in control over electronic transport in a solid-state environment. Correlated electron waveguides offer unique opportunities to investigate the rich physics that is predicted for 1D quantum systems (4). For example, the number of quantum channels can be tuned to the lowest spin-polarized state (with $G = e^2/h$), forming an ideal spin-polarized Luttinger liquid. These 1D channels form a convenient and reproducible starting point for emulating a wider class of 1D quantum systems or for creating quantum channels that can be utilized in a quantum computing platform. While the lowest spin-polarized state is robust to disorder, the higher modes are very sensitive, which makes them potentially useful for nanoscale sensing.

MATERIALS AND METHODS

Sample growth and device fabrication

LaAlO₃/SrTiO₃ samples are grown by pulsed laser deposition (PLD) under conditions that are described in detail elsewhere (45). The electron waveguides are created using c-AFM lithography technique (31, 32). Positive voltages applied between the c-AFM tip and the top LaAlO₃ surface locally produce conductive regions at the LaAlO₃/SrTiO₃ interface (illustrated in Figure 1A), while negative voltages locally restore the insulating phase. The mechanism for writing (erasing) is attributed to LaAlO₃ surface protonation (deprotonation) (46, 47). The protonated LaAlO₃ surface in critical-thickness LaAlO₃/SrTiO₃ heterostructures creates an attractive confining potential that defines the nanowire. Because the protons are physically separated from the conducting region by a highly insulating LaAlO₃ barrier, this nanofabrication method can be viewed as analogous to the “modulation

doping” technique (48) commonly used in III-V semiconductor heterostructures. The separation of dopants from the conducting region minimizes scattering from imperfections. A key difference from III-V nanostructures is the relative proximity between the dopant layer and conducting channel, here only 1.2 nm. Typical nanowire widths at room temperature are $w \sim 10$ nm, as measured by local erasure experiments (31).

The geometry used to investigate electron waveguide transport (Figure 1A) consists of a nanowire channel of total length L_C , surrounded by two narrow, highly transparent barriers (width $L_B \sim 5 - 20$ nm) separated by a distance $L_S \sim 10 - 1000$ nm. The chemical potential μ of the nanowire segment can be tuned by a side-gate voltage V_{sg} , which is positioned about 800 nm away from the nanowire. The wires are written at a tip voltage $V_{tip} = 15$ V except the waveguide, which is created by a two-step voltage sequence. First, we move the AFM tip with $V_{tip} = 8$ V across the LaAlO_3 surface to create the main channel. Next, we repeat the same tip path with a small base voltage ($V_{tip} = 1$ V) and apply two negative voltage pulses ($V_{tip} = -7.5$ V) to create two transparent barriers. The barrier height is determined by the amplitude and duration of the negative pulses. Four-terminal transport measurements are carried out at or close to the base temperature of a dilution refrigerator ($T = 50$ mK) and subject to out-of-plane magnetic fields B .

References and Notes

1. Klitzing Kv, Dorda G, & Pepper M (1980) New Method for High-Accuracy Determination of the Fine-Structure Constant Based on Quantized Hall Resistance. *Phys Rev Lett* 45(6):494-497.
2. Stormer HL, Tsui DC, & Gossard AC (1999) The fractional quantum Hall effect. *Reviews of Modern Physics* 71(2):S298-S305.
3. Luttinger JM (1963) An Exactly Soluble Model of a Many-Fermion System. *Journal of Mathematical Physics* 4(9):1154-1162.
4. Giamarchi T (2003) *Quantum Physics in One Dimension* (Oxford University Press).
5. Auslaender OM, *et al.* (2005) Spin-Charge Separation and Localization in One Dimension. *Science* 308(5718):88-92.
6. Steinberg H, *et al.* (2008) Charge fractionalization in quantum wires. *Nat Phys* 4(2):116-119.
7. Landauer R (1957) Spatial Variation of Currents and Fields Due to Localized Scatterers in Metallic Conduction. *Ibm J Res Dev* 1(3):223-231.
8. van Wees BJ, *et al.* (1988) Quantized conductance of point contacts in a two-dimensional electron gas. *Phys Rev Lett* 60(9):848-850.
9. Wharam DA, *et al.* (1988) One-Dimensional Transport and the Quantization of the Ballistic Resistance. *J Phys C Solid State* 21(8):L209-L214.
10. Yacoby A, *et al.* (1996) Nonuniversal conductance quantization in Quantum wires. *Phys Rev Lett* 77(22):4612-4615.
11. Frank S, Poncharal P, Wang ZL, & Heer WAd (1998) Carbon Nanotube Quantum Resistors. *Science* 280(5370):1744-1746.
12. Lin Y-M, Perebeinos V, Chen Z, & Avouris P (2008) Electrical observation of subband formation in graphene nanoribbons. *Phys Rev B* 78(16):161409.
13. van Weperen I, Plissard SR, Bakkers EPAM, Frolov SM, & Kouwenhoven LP (2013) Quantized conductance in an InSb nanowire. *Nano Lett* 13(2):387-391.
14. Timp G, *et al.* (1987) Quantum transport in an electron-wave guide. *Phys Rev Lett* 59(6):732-735.
15. Haldane FDM (1981) 'Luttinger liquid theory' of one-dimensional quantum fluids. I. Properties of the Luttinger model and their extension to the general 1D interacting spinless Fermi gas. *Journal of Physics C: Solid State Physics* 14(19):2585.
16. Kane CL & Fisher MPA (1992) Transmission through barriers and resonant tunneling in an interacting one-dimensional electron gas. *Phys Rev B* 46(23):15233-15262.
17. Giamarchi T & Schulz HJ (1988) Anderson localization and interactions in one-dimensional metals. *Phys Rev B* 37(1):325-340.
18. Tsukazaki A, *et al.* (2010) Observation of the fractional quantum Hall effect in an oxide. *Nat Mater* 9(11):889-893.

19. Falson J, *et al.* (2015) Even-denominator fractional quantum Hall physics in ZnO. *Nat Phys* 11(4):347-351.
20. Ohtomo A & Hwang HY (2004) A high-mobility electron gas at the LaAlO₃/SrTiO₃ heterointerface. *Nature* 427(6973):423-426.
21. Thiel S, Hammerl G, Schmehl A, Schneider CW, & Mannhart J (2006) Tunable quasi-two-dimensional electron gases in oxide heterostructures. *Science* 313(5795):1942-1945.
22. Reyren N, *et al.* (2007) Superconducting interfaces between insulating oxides. *Science* 317(5842):1196-1199.
23. Brinkman A, *et al.* (2007) Magnetic effects at the interface between non-magnetic oxides. *Nature Materials* 6(7):493-496.
24. Irvin P, *et al.* (2013) Anomalous High Mobility in LaAlO₃/SrTiO₃ Nanowires. *Nano Lett* 13(2):364.
25. Cheng G, *et al.* (2013) Anomalous Transport in Sketched Nanostructures at the LaAlO₃/SrTiO₃ Interface. *Physical Review X* 3(1):011021.
26. Ron A & Dagan Y (2014) One-dimensional Quantum wire formed at the boundary between two insulating LaAlO₃/SrTiO₃ interfaces. *Phys Rev Lett* 112(13):136801.
27. Tomczyk M, *et al.* (2016) Micrometer-scale ballistic transport of electron pairs in LaAlO₃/SrTiO₃ nanowires. *Phys Rev Lett* 117(9):096801.
28. Datta S (2013) *Quantum transport : atom to transistor* (Cambridge University Press, Cambridge, UK ; New York) Repr. with corrections. Ed pp xiv, 404 pages.
29. Maslov DL & Stone M (1995) Landauer conductance of Luttinger liquids with leads. *Phys Rev B* 52(8):R5539-R5542.
30. Nikolić K & MacKinnon A (1994) Conductance and conductance fluctuations of narrow disordered quantum wires. *Phys Rev B* 50(15):11008-11017.
31. Cen C, *et al.* (2008) Nanoscale control of an interfacial metal-insulator transition at room temperature. *Nature Materials* 7(4):298-302.
32. Levy A, *et al.* (2014) Writing and Low-Temperature Characterization of Oxide Nanostructures. *Journal of Visualized Experiments* 89:e51886.
33. Micolich AP (2011) What lurks below the last plateau: experimental studies of the $0.7 \times 2 e^2 / h$ conductance anomaly in one-dimensional systems. *Journal of Physics: Condensed Matter* 23(44):443201.
34. Bi F, *et al.* (2016) Electro-mechanical response of top-gated LaAlO₃/SrTiO₃. *J Appl Phys* 119(2):025309.
35. Salluzzo M, *et al.* (2009) Orbital Reconstruction and the Two-Dimensional Electron Gas at the LaAlO₃/SrTiO₃ Interface. *Phys Rev Lett* 102(16):166804.
36. Topinka MA, *et al.* (2000) Imaging Coherent Electron Flow from a Quantum Point Contact. *Science* 289(5488):2323-2326.
37. Cheng G, *et al.* (2015) Electron pairing without superconductivity. *Nature* 521(7551):196.

38. Guan X-W, Batchelor MT, & Lee C (2013) Fermi gases in one dimension: From Bethe ansatz to experiments. *Reviews of Modern Physics* 85(4):1633-1691.
39. Wang B, Chen H-D, & Das Sarma S (2009) Quantum phase diagram of fermion mixtures with population imbalance in one-dimensional optical lattices. *Phys Rev A* 79(5):051604.
40. Orso G, Burovski E, & Jolicoeur T (2010) Luttinger Liquid of Trimers in Fermi Gases with Unequal Masses. *Phys Rev Lett* 104(6):065301.
41. Maslov DL (1995) Transport through dirty Luttinger liquids connected to reservoirs. *Phys Rev B* 52(20):R14368-R14371.
42. Sawada A, *et al.* (1998) Phase Transition in the $\nu=2$ Bilayer Quantum Hall State. *Phys Rev Lett* 80(20):4534-4537.
43. Beenakker CWJ & van Houten H (1991) Josephson current through a superconducting quantum point contact shorter than the coherence length. *Phys Rev Lett* 66(23):3056-3059.
44. Kanasz-Nagy M, Glazman L, Esslinger T, & Demler EA (2016) Anomalous conductances in an ultracold quantum wire. (arXiv:1607.02509).
45. Cheng G, *et al.* (2011) Sketched oxide single-electron transistor. *Nat Nanotechnol* 6(6):343-347.
46. Brown KA, *et al.* (2016) Giant conductivity switching of $\text{LaAlO}_3/\text{SrTiO}_3$ heterointerfaces governed by surface protonation. *Nature Communications* 7:10681.
47. Bi F, *et al.* (2010) "Water-cycle" mechanism for writing and erasing nanostructures at the $\text{LaAlO}_3/\text{SrTiO}_3$ interface. *Applied Physics Letters* 97(17):173110.
48. Dingle R, Stormer HL, Gossard AC, & Wiegmann W (1978) Electron Mobilities in Modulation-Doped Semiconductor Heterojunction Super-Lattices. *Applied Physics Letters* 33(7):665-667.

Acknowledgments

We thank Andrew Daley and Ben Hunt for valuable discussions. This work was supported by ONR N00014-15-1-2847 (J.L.), AFOSR FA9550-15-1-0334 (C.B.E.), AFOSR FA9550-12-1-0057 (J.L., C.B.E.), AOARD FA2386-15-1-4046 (C.B.E.) and grants from the National Science Foundation DMR-1104191 (J.L.), DMR-1124131 (C.B.E., J.L.) and DMR-1629270 (C.B.E.).

Supporting Information for

Quantized Ballistic Transport of Electrons and Electron Pairs in LaAlO₃/SrTiO₃ Nanowires

Anil Annadi, Guanglei Cheng, Hyungwoo Lee, Jung-Woo Lee, Shicheng Lu, Anthony Tylan-Tyler, Megan Briggeman, Michelle Tomczyk, Mengchen Huang, David Pekker, Chang-Beom Eom, Patrick Irvin, Jeremy Levy

Table of Contents:

- Section S1. Finite bias spectroscopy
- Section S2. Estimation of ballistic scattering length
- Section S3. Impact of side gate location
- Section S4. Tight-binding Hamiltonian for electron waveguide
- Section S5. Avoided crossings
- Section S6. Other devices
- Section S7. Single barrier vs. double barrier geometry
- Figure S1. Finite bias analysis
- Figure S2. Quantization of the $1 e^2/h$ plateau
- Figure S3. Effect of gate geometry
- Figure S4. Critical magnetic field for splitting the lowest two spin subbands for additional devices D and E
- Figure S5. Representative transport data of a device with only one barrier
- Table S1. Measured scattering lengths and standard errors for Device A and B
- Table S2. Avoided crossing fitting parameters for device A and B
- References (49-53)

Section S1. Finite bias spectroscopy

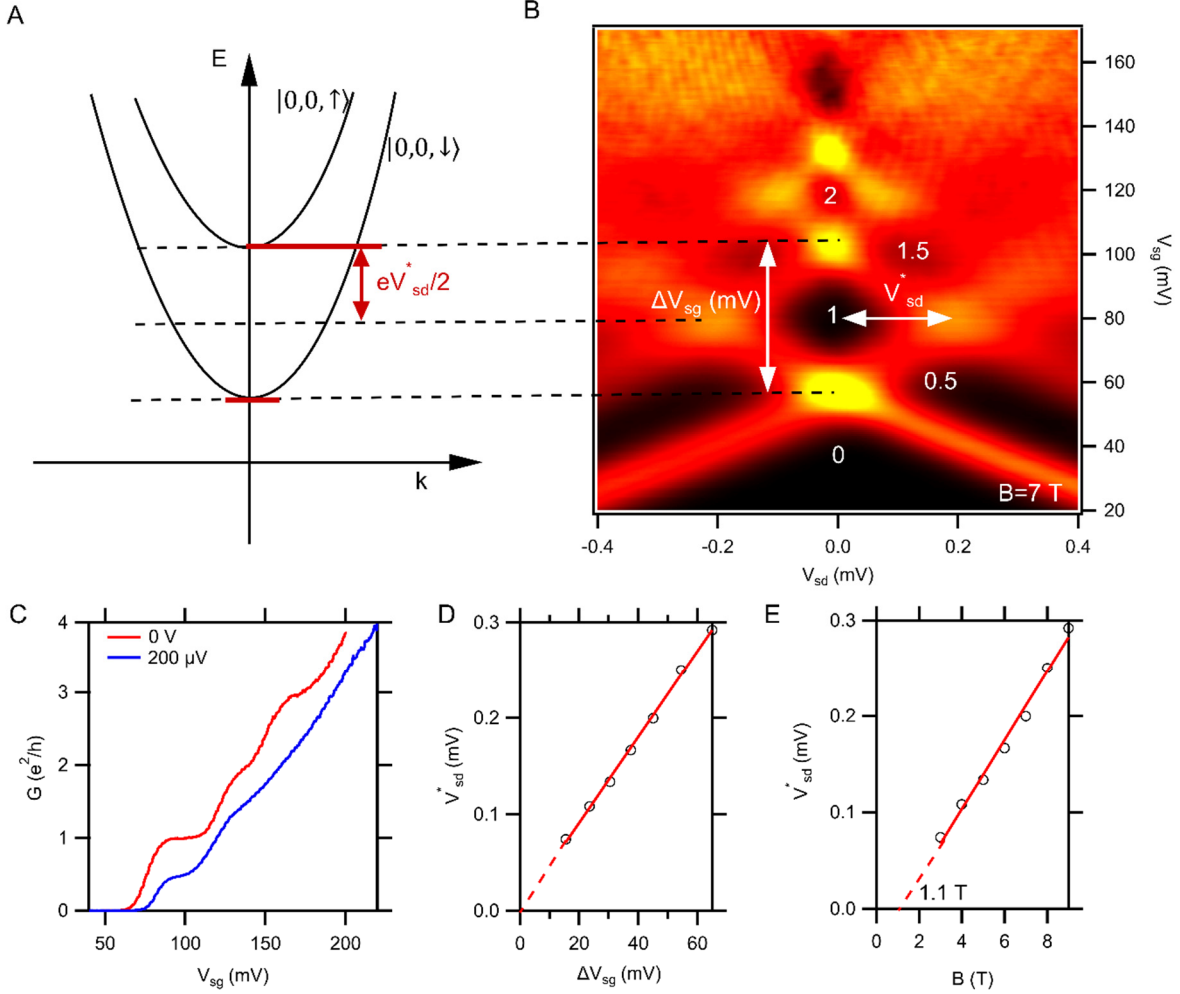


Figure S1. Finite bias analysis. (A) Illustration of electron occupation of subbands $|0,0,\downarrow\rangle$ and $|0,0,\uparrow\rangle$ at a finite bias V_{sd} in a magnetic field $B = 7$ T. The application of V_{sd} alters the chemical potentials of drain (μ_d) and source (μ_s) to $E_F \pm eV_{sd}/2$. The energy difference $\mu_d - \mu_s = eV_{sd}$ (as indicated by two red lines) equals the subband spacing between subbands $|0,0,\downarrow\rangle$ and $|0,0,\uparrow\rangle$. When $V_{sd} < V_{sd}^*$, electrons travelling in opposite directions occupy the same subband $|0,0,\downarrow\rangle$ with conductance quantized to e^2/h . When V_{sd} reaches $|V_{sd}^*|$ ($-|V_{sd}^*|$), subband $|0,0,\uparrow\rangle$ becomes available for electrons transmitting from drain (source) and gives rise to half plateau conductance ($1.5 e^2/h$). (B) Transconductance map of device A as a function of V_{sd} and V_{sg} at $B = 7$ T. Each dark band marks the transition between conductance plateaus which are labelled by blue numbers. According to a, the conversion factor α can be extracted through a simple relation $V_{sd}^* = \alpha \Delta V_{sg}$. (C) G vs V_{sg} curves of zero bias ($V_{sd} = 0$ V) and finite bias ($V_{sd} = V_{sd}^* = 200$ μ V) at $B = 7$ T. Half plateaus are clearly visible at finite bias (blue curve). (D) V_{sd}^* dependent on ΔV_{sg} at magnetic fields from 3 T to 9 T in step of 1 T. The linear relationship and negligible intercept clearly establishes $V_{sd}^* = \alpha \Delta V_{sg}$ with $\alpha = 4.5$ μ eV/mV. (E) Zeeman splitting between subbands $|0,0,\downarrow\rangle$ and $|0,0,\uparrow\rangle$ with the same field variation in (D). The g factor can be extracted to be $g = 0.6$.

Remarkably, subbands $|0,0,\downarrow\rangle$ and $|0,0,\uparrow\rangle$ only split above a critical magnetic field $B_p = 1.1$ T, which is marked by the intercept in the B axis.

Finite-bias spectroscopy is performed through current-voltage (I - V) measurements as function of V_{sg} and B to gain more information of the electron waveguides. As shown in Figure S1A, a large finite bias ($V_{sd} \geq V_{sd}^*$) can unevenly populate subbands occupied by oppositely travelling electrons, which gives rise to the so-called half plateaus (49, 50). Figure S1B is the finite-bias transconductance plot of device A at $B = 7$ T. The dark regions marked by the numbers are where conductance is quantized. The $0.5e^2/h$ and $1.5e^2/h$ plateaus can be clearly seen in the conductance plot at $V_{sd} = V_{sd}^* = 200$ μ V (Figure S1C). The observation of these half plateaus is indicative of very clean transport of the electron waveguide devices, since back scattering is more likely to happen when unoccupied subbands become available at finite biases.

Finite-bias spectroscopy is used to extract the lever-arm α , which converts gate voltage to chemical potential. As illustrated in Figure S1B, the bright crossing ($V_{sd}^* = 200$ μ V, $V_{sg} = 80$ mV) marks the transition from one subband to another due to the bias. At this condition, the energy gain induced by the bias V_{sd}^* should equal to subband spacing marked by $\alpha\Delta V_{sg}$ at zero bias, namely $eV_{sd} = \alpha\Delta V_{sg}$. Then $\alpha = eV_{sd}^*/\Delta V_{sg}$ can be precisely extracted by the slope of the $V_{sd}^* - \Delta V_{sg}$ plot at different magnetic fields (Figure S1D). For device A, α_A is found to 4.5 μ eV/mV, and the fitted linear curve passes across zero as supposed. Similarly, $\alpha_B = 9.9$ μ eV/mV can be extracted for device B, suggesting a stronger coupling of side gate to the waveguide due to the larger size.

The Zeeman splitting between two spin-resolved subbands $|0,0,\uparrow\rangle$ and $|0,0,\downarrow\rangle$ can be used to extract the electron g factor. Figure S1D shows the energy splitting (eV_{sd}^*) between these

two subbands at various magnetic fields, where spin degeneracy is moved. Then the g factor is given by $g = \frac{eV_{sd}^*}{\mu_B B}$, where μ_B is the Bohr magneton. And the extracted g factors for device

A and B are (within measurement error) the same: $g_{A(B)} = 0.6$.

Section S2. Estimation of ballistic scattering length

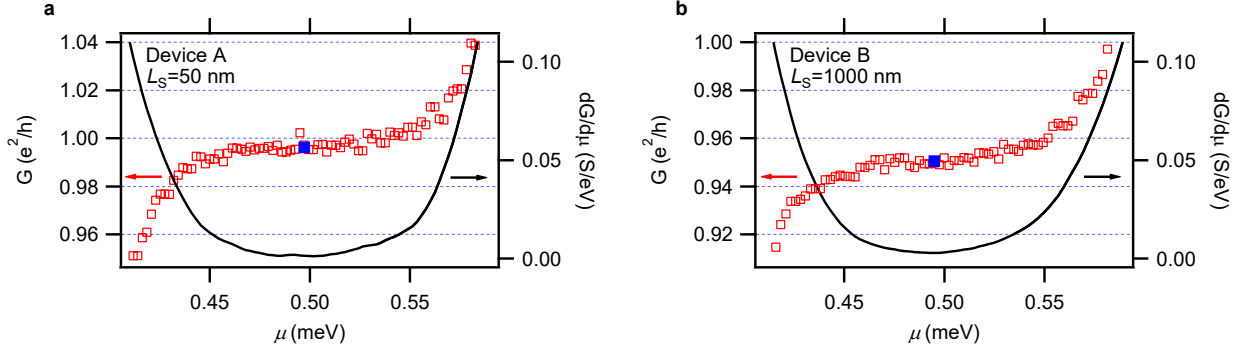


Figure S2. Quantization of the $1e^2/h$ plateau. (A) The first conductance plateau and transconductance for device A. (B) The first conductance plateau and transconductance for Device B. For both devices, a fit to the conductance at the minimum of the transconductance is used to estimate scattering lengths.

Table S1. Measured scattering lengths and standard errors for Device A and B, based on deviations from precise quantization Ne^2/h of conduction.

Device	Plateau N	L (nm)	ΔL (nm)	$G(e^2/h)$	$\Delta G(e^2/h)$	$L_0(\mu m)$	$\delta L_0(\mu m)$
A	1	50	10	0.995	0.004	10	8
A	2	50	10	0.964	0.12	2	14
B	1	1000	10	0.955	0.003	21.7	1.4
B	2	1000	10	0.899	0.076	7.8	4.6

Section S3. Impact of side gate location

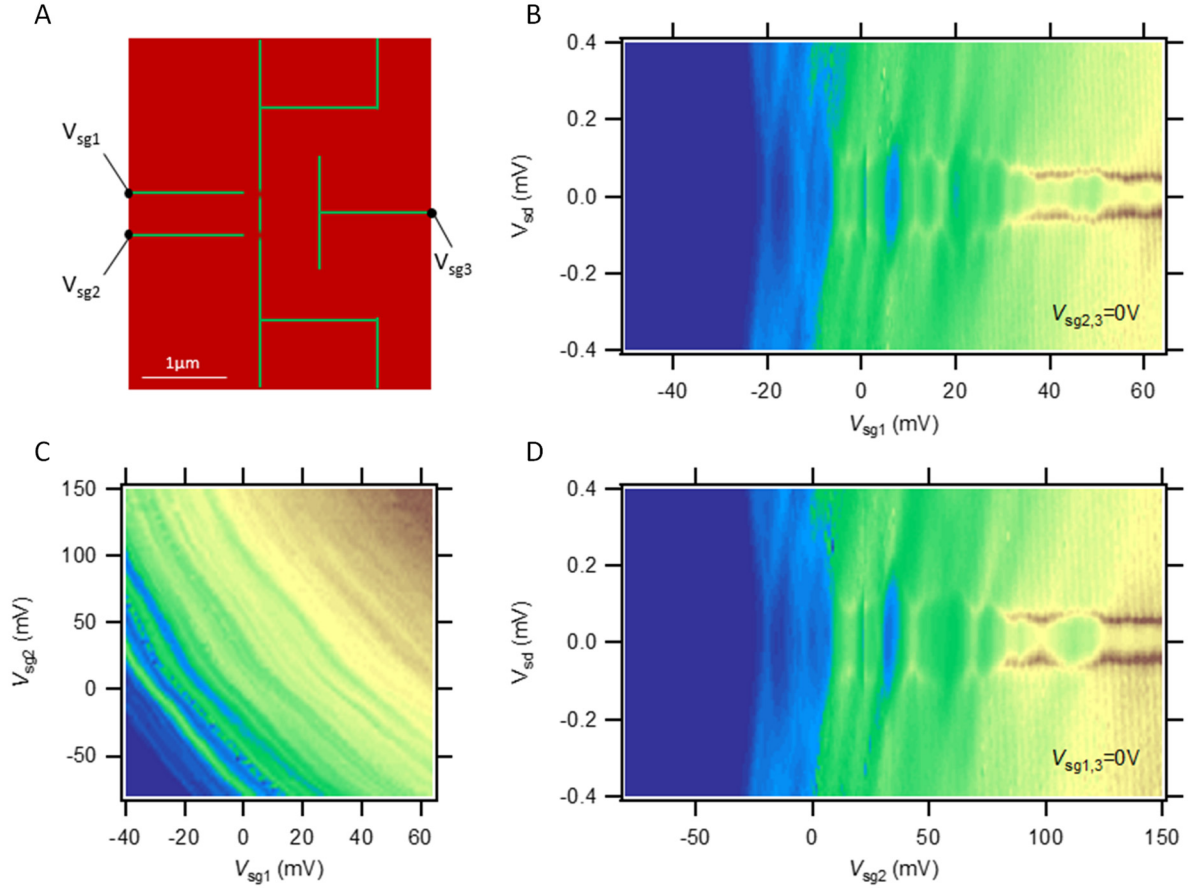


Figure S3. Effect of gate geometry. (A) Illustration of triple-gate device, consisting of two large tunneling barriers in the main channel, two point-gates near each dot (V_{sg1} and V_{sg2}), and a long middle gate to universally tune the device (V_{sg3}). (B) Conductance measured by lock-in technique as a function of V_{sg1} and V_{sg2} , with V_{sg3} floating. While the lever arm for each gate is different, the conductance features exhibit highly similar dependence on gate voltage, regardless of which gate is swept. (C-D) Conductance dI/dV as a function of source-drain bias V_{sd} and either V_{sg1} (C) or V_{sg2} (D) while holding the other two gates constant at 0 V.

The physical location of the side gates for $\text{LaAlO}_3/\text{SrTiO}_3$ nanostructures affect the overall lever arm but, somewhat surprisingly, does not appear to impact the electronic structure within the conducting regions. To illustrate, we show transport results for a single-electron transistor device with multiple side gates (Figure S3A). The differential conductance is shown as a function of four-terminal source-drain voltage V_{sd} and either of the side gates located near one or the other barrier (V_{sg1} or V_{sg2}). The results for both gates are nearly

identical (Figure S3C, D), which shows that the electric fields are effectively screened and the main result of gating is to change the chemical potential uniformly within the conducting wire segment. The near equivalence of both gates is also shown by plotting the conductance at zero bias versus the two gates (Figure S3B). Differences between the two gates are negligibly small, apart from the factor-of-two difference in lever arms. This insensitivity is likely related to the very large dielectric constant of SrTiO₃ at low temperatures.

Section S4. Tight-binding Hamiltonian for electron waveguide

As the magnetic field couples to motion in the xy -plane, the characteristic length scale and mass in the y -direction may be extracted directly from the transconductance data. To extract l_z and m_z^* from ω_z , it is necessary to use a more complete tight-binding model which includes the atomic spin-orbit coupling between the 3 Ti t_{2g} orbitals. The inclusion of this term then allows us to vary the mass m_z^* of the d_{xy} band (and the corresponding masses of the d_{yz} and d_{zx} bands) to see the reduction in the electron g factor (see later discussion in Sec. V). The resulting tight-binding Hamiltonian takes the form

$$\begin{aligned}
H = \sum_{i,j,k} \left[\sum_{\alpha,s} \left(-t_x^\alpha e^{\frac{i\phi_B j d^2}{\phi_0}} a_{i,j,k}^{\alpha s \dagger} a_{i+1,j,k}^{\alpha s} - t_y^\alpha a_{i,j,k}^{\alpha s \dagger} a_{i,j+1,k}^{\alpha s} - t_z^\alpha a_{i,j,k}^{\alpha s \dagger} a_{i,j,k+1}^{\alpha s} \right) \right. \\
+ \frac{\Delta_{aso}}{2} \sum_{s,s'} \left(-i\sigma_y^{ss'} a_{i,j,k}^{d_{xy}s'\dagger} a_{i,j,k}^{d_{yz}s'} + i\sigma_x^{ss'} a_{i,j,k}^{d_{xy}s'\dagger} a_{i,j,k}^{d_{xz}s'} \right. \\
\left. \left. + i\sigma_z^{ss'} a_{i,j,k}^{d_{yz}s'\dagger} a_{i,j,k}^{d_{xz}s'} \right), +h.c. \right] \\
+ \sum_{i,j,k,s,\alpha} \left[\left(\frac{m_y^{d_{xy}*} \omega_y^2}{2} (jd)^2 + \frac{m_z^{d_{xy}*} \omega_z^2}{2} (kd)^2 + 2t_x^\alpha + 2t_y^\alpha \right. \right. \\
\left. \left. + 2t_z^\alpha \right) a_{i,j,k}^{\alpha s \dagger} a_{i,j,k}^{\alpha s} + \frac{g}{2} \mu_B B \sigma_z a_{i,j,k}^{\alpha s \dagger} a_{i,j,k}^{\alpha s} \right]
\end{aligned} \tag{S1}$$

where t_i^α is the hopping in the i -direction for the band α , d is the lattice constant, ϕ_0 is the magnetic flux quantum, $\Delta_{aso} = 19.3\text{meV}$ is the atomic spin-orbit coupling (51), g is the bare-electron g factor, μ_B is the Bohr magneton, and $a_{i,j,k}^{\alpha s(\dagger)}$ destroys (creates) an electron at site i, j, k with spin s in band α . From this, the effective g factor can be extracted and compared to the experimental value to extract l_z and m_z^* from ω_z .

Section S5. Avoided crossings

Experimentally, we observe that when two subbands $|n_1, m_1, s\rangle$ and $|n_2, m_2, s\rangle$ share the same spin quantum number s and are nearly degenerate in energy ($E_{m_1, n_1, s} \approx E_{m_2, n_2, s}$), e.g., $|1, 0, \uparrow\rangle$ and $|0, 1, \uparrow\rangle$, they form an avoided crossing (Figure 5). It is tempting to associate avoided crossings with repulsive electron-electron interactions, however the phase diagram of the repulsive version of the model (Eq. (4)) does not admit this interpretation. However, an avoided crossing arises naturally if the transverse confinement potential is not separable

(52, 53). To model these avoided crossings, a simple two-level effective Hamiltonian of the form

$$H_{\text{eff}} = \begin{pmatrix} E_1 & \Delta_{1,2} \\ \Delta_{1,2} & E_2 \end{pmatrix} \quad (\text{S2})$$

is used, where $\Delta_{1,2}$ models the non-separability of the confinement potential by coupling the two states E_1 and E_2 . The chemical potentials at which the two transverse subbands become occupied follows:

$$E_{AV\pm} = \frac{1}{2}(E_1 + E_2) \pm \frac{1}{2}\sqrt{(E_1 - E_2)^2 + 4\Delta_{1,2}^2} \quad (\text{S3})$$

To fit the experimental data, and extract the parameter $\Delta_{1,2}$, we approximate the single particle energy eigenvalue E_i with a linear magnetic field dependence $E_i = k_i B + b_i$ in the vicinity of the avoided crossing (see Figure 5, as well as Table S).

Table S2. Avoided crossing fitting parameters for device A and B.

Device	Subbands	k ($\mu\text{eV/T}$)	b (μeV)	$\Delta_{1,2}$ (μeV)
Device A	$ 1,0,\uparrow\rangle$	167	8	20
	$ 0,1,\uparrow\rangle$	58	534	
	$ 1,0,\downarrow\rangle$	91	195	16
	$ 0,1,\downarrow\rangle$	15	566	
Device B	$ 1,0,\uparrow\rangle$	166	-58	34
	$ 0,1,\uparrow\rangle$	63	529	
	$ 1,0,\downarrow\rangle$	95	139	40
	$ 0,1,\downarrow\rangle$	14	585	

Section S6. Other devices

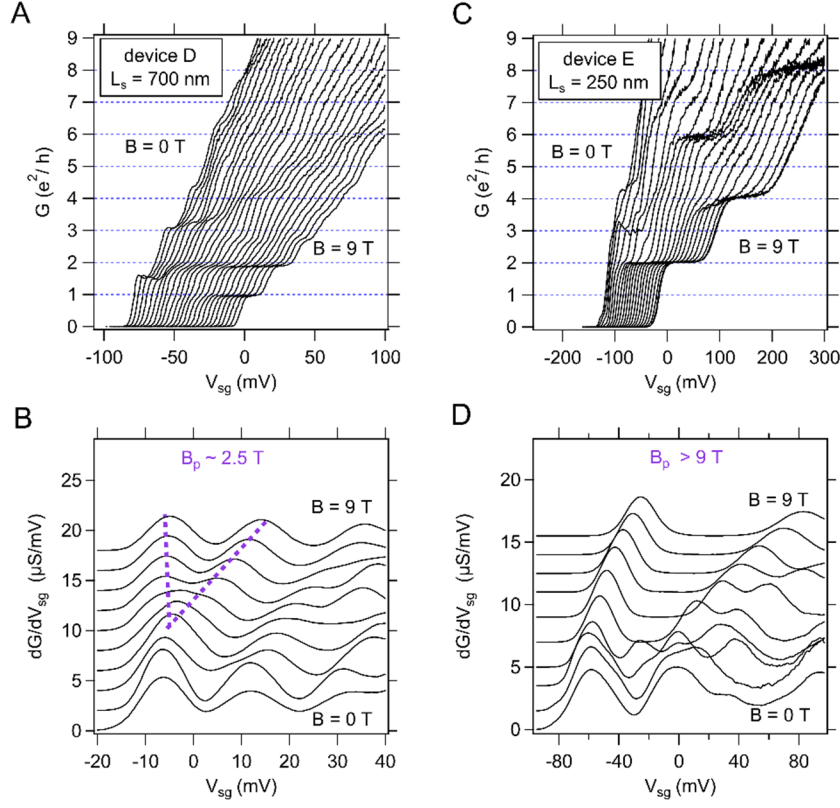


Figure S4. Critical magnetic field for splitting the lowest two spin subbands for additional devices D and E (A and C). Zero-bias conductance G as a function of V_{sg} and B for device D ($L_B = 20$ nm, $L_C = 1500$ nm, $L_S = 700$ nm) and E ($L_B = 20$ nm, $L_C = 500$ nm, $L_S = 250$ nm) fabricated on different samples. Curves are offset for clarity (B and D). Corresponding transconductance dG/dV_{sg} plots to reveal B_p at which subbands $|0,0,\downarrow\rangle$ and $|0,0,\uparrow\rangle$ start to split. B_p values are high for device D (~ 2.5 T) and E (> 9 T) compared to device A and B in the main text.

Section S7. Single barrier vs. double barrier geometry

In GaAs-based heterostructure devices, the number of transverse channels that are transmitted through a quantum point contact is typically controlled by a split top gate. Varying the potential on the split top gate then controls the effective width of the conducting region. In the case of $\text{LaAlO}_3/\text{SrTiO}_3$, similar behavior may be expected in the case where a side gate is used to control a quantum point contact created by a single weak barrier. In Figure S5, we show the results of varying the V_{sg} for a device with a single barrier in the channel. At all values of the magnetic field, there is no clear quantization of the conductance. This is consistent with the single-particle theory shown in Figs. 2, 3 which holds the width of the conducting channel, ℓ_y , fixed as V_{sg} is varied. Thus we conclude that, as in the case for the quantum dot geometries used in Ref [41], varying V_{sg} controls the chemical potential of the region between the barriers, as illustrated in Figure 1.

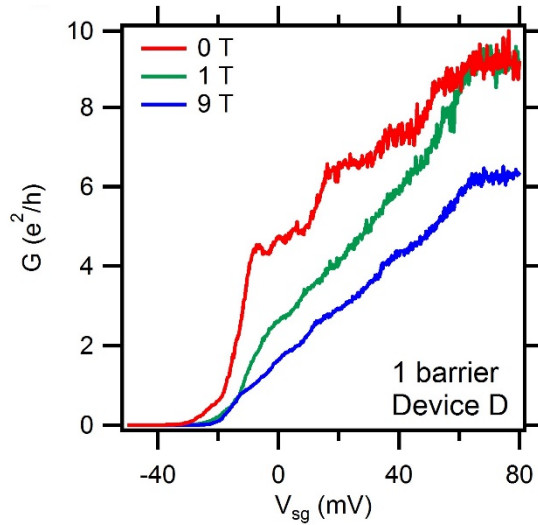


Figure S5. Representative transport data of a device with only one barrier. No conductance quantization is observed.

- 49. Glazman LI & Khaetskii AV (1989) Nonlinear Quantum Conductance of a Lateral Microconstraint in a Heterostructure. *Europhys Lett* 9(3):263-267.
- 50. Patel NK, *et al.* (1990) Ballistic transport in one dimension: additional quantisation produced by an electric field. *Journal of Physics: Condensed Matter* 2(34):7247.
- 51. Zhong ZC, Toth A, & Held K (2013) Theory of spin-orbit coupling at $\text{LaAlO}_3/\text{SrTiO}_3$ interfaces and SrTiO_3 surfaces. *Phys Rev B* 87(16):161102.
- 52. Salis G, *et al.* (1999) Mode spectroscopy and level coupling in ballistic electron waveguides. *Phys Rev B* 60(11):7756-7759.
- 53. Fischer SF, Apetii G, Kunze U, Schuh D, & Abstreiter G (2005) Magnetotransport spectroscopy of spatially coincident coupled electron waveguides. *Phys Rev B* 71(19):195330.